Probing the Suitability of Meridional Stratospheric Ozone Gradients for Inferring Interannual Variability and Trends of the Subtropical Jet Stream

FREDERIK HARZER,[a] HELLA GARNY,[b,a] SEAN DAVIS,[c] AND THOMAS BIRNER[a,b]

[a] *Meteorological Institute, Ludwig-Maximilians-Universität München, Munich, Germany*
[b] *Institute of Atmospheric Physics, Deutsches Zentrum für Luft- und Raumfahrt, Oberpfaffenhofen, Germany*
[c] *NOAA/Chemical Sciences Laboratory, Boulder, Colorado*

(Manuscript received 17 September 2024, in final form 31 January 2025, accepted 18 February 2025)

ABSTRACT: Atmospheric jet streams belong to the most fundamental elements of the global general circulation system and are susceptible to climate change. Jet stream variability in our present climate is usually studied from modern reanalysis products, although uncertainties arise due to insufficiently strong constraints of the underlying global wind field by the available observational records, especially concerning their long-term trends. This motivates the use of observation-based metrics to track dynamical variability and historical trends. Here, we investigate how the zonal-mean ozone structure can be used to indirectly infer changes in the strength and latitudinal position of the subtropical jet streams (STJs). We mainly consider the winter-mean ozone distribution and analyze different diagnostics that track anomalies of the sharp ozone gradients near the subtropical tropopause, based on either vertically resolved or total-column ozone (TCO) fields. Using ERA5 reanalysis output, we find significant correspondence of these sharp ozone gradients with the STJ's strength and location, with the jet acting as a tracer transport barrier and, hence, governing wave-induced horizontal ozone transport across the jet core. The ozone gradient metrics obtained from vertically resolved ozone observations agree well with ERA5 in more recent years when densely sampled satellite measurements were included. We furthermore obtain mostly consistent historical trend signals from both conventional STJ metrics from reanalyses and more independent TCO records. Chemistry–Climate Model Initiative phase 1 (CCMI-1) and CMIP6 climate simulations suggest a strong correspondence between changes in subtropical ozone gradient maxima and projected STJ trends under different climate forcing scenarios.

KEYWORDS: Atmospheric circulation; Jets; Ozone; Interannual variability; Trends

1. Introduction

Climate research has provided evidence for robust climate change signatures of the large-scale atmospheric general circulation as the response to increasing levels of greenhouse gas concentrations (e.g., Shaw et al. 2024; Lee et al. 2021; Schneider 2006). In particular, generations of climate projections suggest a robust strengthening of the strong eastward winds located along the subtropical tropopause break in both hemispheres, usually referred to as the subtropical jet streams (STJs), which is consistent with enhanced meridional temperature gradients in the subtropical upper troposphere and lower stratosphere (UTLS) under climate change (e.g., Vallis et al. 2015; Shaw and Miyawaki 2024). Changes in the STJ strength and position further play a key role to drive changes in the (lower) stratospheric circulation, e.g., via regulating wave driving of the shallow branch of the stratospheric Brewer–Dobson circulation and quasihorizontal transport in the UTLS region (Shepherd and McLandress 2011; Abalos and de la Cámara 2020).

The STJs also have been discussed to provide a measure of the latitudinal extent of the tropical belt, albeit their covariability with the tropical overturning Hadley circulation turned out to be rather limited (Staten et al. 2018; Menzel et al. 2019, 2024). Furthermore, the STJ is known to be dynamically linked with the eddy-driven jet (EDJ) stream in the midlatitudes in both hemispheres (e.g., Lee and Kim 2003). This correspondence is clearly reflected, e.g., by the leading mode of intrinsic extratropical variability, which corresponds to latitudinal shifts in the location of the EDJ that project onto the strength of the STJ (Thompson and Wallace 1998, 2000; Limpasuvan and Hartmann 1999). Consistent with the STJ response, robust evidence was found for the poleward shifting of the EDJ in both hemispheres and the strengthening of the Austral midlatitude jet under climate change, with potential implications on the hemispheric storm tracks and extreme synoptic weather events (e.g., Woollings 2016; Shaw 2019; Zappa 2019).

Climate change signals, spanning the last few decades, have started to emerge from historical climate variability (e.g., Totz et al. 2018; Chemke and Yuval 2023; Woollings et al. 2023). The associated wind field variations characterizing the large-scale circulation patterns are often studied using recent reanalysis products that provide highly resolved geophysical model data and that benefit from assimilation through meteorological observations. These wind field components are effectively constrained by temperature through the thermal wind relation, but this constraint may not be sufficiently

Denotes content that is immediately available upon publication as open access.

Supplemental information related to this paper is available at the Journals Online website: https://doi.org/10.1175/JCLI-D-24-0530.s1.

Corresponding author: Frederik Harzer, frederik.harzer@physik.lmu.de

DOI: 10.1175/JCLI-D-24-0530.1

strong for long-term trends and the lack of broadly distributed and regular wind measurements prevents more accurate wind assimilation. Long et al. (2017, 2022) assessed this zonal wind and temperature output from reanalyses and especially for the more recent reanalysis products found overall good agreement, with substantial improvements due to new observational data and advanced measurement systems that became available over time. However, the authors pointed out considerable uncertainties in long-term trend evaluation from reanalyses due to changing observational constraints over time and different procedures to assimilate the observational data. Examining historical Hadley circulation trends, Grise et al. (2019) further emphasized that substantial trend uncertainties are caused by large intrinsic variability in combination with the still rather narrow time frame considered for historical trend analyses. In contrast, interannual atmospheric variability commonly features more consistent signals across datasets and therefore should be less affected by systematic biases in the reanalysis data. This highlights the relevance of modern reanalyses for understanding the atmosphere's internal mechanisms and interconnections from the perspective of both state-of-the-art atmospheric modeling and various types of global observations.

Additional observation-based metrics of jet stream variability may account for some of the above issues and may help to improve the evaluation of relevant general circulation features from reanalysis data. In particular, trend uncertainties may be reduced by choosing indirect metrics that feature reduced intrinsic variability and by using high-quality observational data that minimize inconsistencies due to the measurement setup and during data processing. Here, we propose exploiting atmospheric trace gas distributions to derive tracer-based diagnostics of variability and long-term circulation change. In particular, we consider the ozone distribution in the UTLS region, which is known to be shaped by the transport barrier associated with the STJ and has been found to not be affected much by chemistry in the UTLS. Hudson et al. (2003, 2006) and Hudson (2012) previously used the correspondence between characteristics in the structure of total-column ozone (TCO) and the locations of the atmospheric jets in the Northern Hemisphere to indirectly detect circulation trends. Davis et al. (2018) discussed the limitations of TCO as a tropical width metric due to the generally weak meridional TCO gradients, although they did not examine vertically resolved ozone metrics or TCO-based metrics during seasons with the strongest gradients (e.g., boreal winter).

In this study, we present a class of ozone metrics intended for investigations of jet stream variability in the past climate based on observational data but also applicable to future climate projections by climate models. These metrics are derived from the strong meridional gradients of the zonal-mean ozone distribution in the STJ regions and can be used with both vertically resolved ozone fields as well as TCO profiles. Section 2 lists the data and methods used in this work, and section 3 describes the methodology for computing the ozone-based diagnostics. In section 4, we use data from the fifth major global reanalysis produced by ECMWF (ERA5) to discuss the physical background of the statistical correspondence between zonal-mean ozone and STJ variability. The features and limitations of applying the proposed ozone gradient metrics to observational data are explored in section 5 using vertically resolved ozone observations and TCO records. Finally, in section 6, we compare trend projections for STJ and ozone variability based on the Chemistry–Climate Model Initiative phase 1 (CCMI-1) and phase 6 of the Coupled Model Intercomparison Project (CMIP6) climate simulations. Section 7 contains the summary and discussion of our results.

2. Data and methods

a. Data

We use monthly averaged, zonal-mean ERA5 atmospheric reanalysis data for the years 1979–2023, which was provided on 37 pressure levels between 1 and 1000 hPa with 1° meridional resolution (Hersbach et al. 2020, 2023a,b). In ERA5, a linear ozone parameterization scheme by Cariolle and Teyssèdre (2007) is implemented (ECMWF 2016). Despite the known limitations due to modeling and data assimilation, which require a careful evaluation of the reanalysis output, ERA5 was shown to perform reasonably well in reproducing the observed variability in the vertically resolved ozone distribution (Davis et al. 2022).

For comparing historical STJ and EDJ trends, we also use monthly mean data from three additional reanalyses: combined CFSR (through 2010) and CFSv2 (from 2010), Japanese Reanalysis for three quarters of a century (JRA-3Q), and MERRA-2, each for the time period 1980–2019 with 2.5° meridional resolution, which all were provided through the "Reanalysis Intercomparison Dataset" (RID) prepared by the SPARC Reanalysis Intercomparison Project (S-RIP; using updated data by Martineau et al. 2018). Note that here, for consistent zonal averaging of the 850-hPa zonal wind field, we masked out all data in these three reanalyses that correspond to data points below ground in MERRA-2 and therefore were missing in the MERRA-2 output, mainly located in the American and Asian high mountain regions and covering most parts of Greenland and the Antarctic continent.

In section 5, we evaluate "Stratospheric Water and Ozone Satellite Homogenized" ("SWOOSH") version 2.6 data produced by Davis et al. (2016). Starting in 1984, this dataset provides monthly averaged zonal-mean ozone distributions, merged from different observational instruments and interpolated on 31 pressure levels between 1 and 316 hPa with 2.5° meridional resolution. Furthermore, we consider zonally averaged TCO data from the ESA Climate Change Initiative (CCI) multisensor reanalysis (MSR), covering the years 1970–2022 with 0.5° meridional resolution (Copernicus Climate Change Service 2020; Van Roozendael et al. 2021a,b). We compare them with the "BS Filled Total Column Ozone Database" version 3.4.1 (monthly means, 1978–2019, 1° meridional resolution) by Bodeker et al. (2021, 2022).

We also consider zonal-mean, monthly averaged model output from 18 CCMI-1 climate simulations (Eyring et al. 2013; Hegglin et al. 2015) listed in Table 1. With two exceptions,

TABLE 1. CCMI-1 and CMIP6 simulations together with the number of ensemble members considered in this work.

CCMI-1	REF-C1	REF-C2
ACCESS CCM	1	2
CCSRNIES MIROC3.2	3	2
CESM1 CAM4-chem	3	3
CESM1(WACCM)	3	3
CHASER (MIROC-ESM)	·	1
CMAM	3	1
CNRM-CM5-3	1	1
EMAC (L47MA)	1	3
EMAC (L90MA)	1	1
GEOSCCM	1	1
GFDL-CM3	5	1
GRIMs-CCM	1	·
MOCAGE	1	1
MRI-ESM1r1	1	1
NIWA-UKCA	3	5
SOCOL	3	1
UMSLIMCAT	1	1
UMUKCA-UCAM	1	2
CMIP6	**SSP2-4.5**	**SSP5-8.5**
CESM2(WACCM)[a]	3	3
CNRM-ESM2-1	3	3
GFDL-ESM4	1	1
MRI-ESM2.0	1	1
UKESM1.0-LL	3	3

[a]No TCO data available.

all of these models provided data for both a free-running hindcast simulation ("REF-C1," 1960–2010) using historical observations, as well as for a projection run "REF-C2" (1960–2100) that is based on the WMO A1 scenario on ozone-depleting substances from 2011 combined with the CMIP5 representative concentration pathway (RCP) 6.0 (Eyring et al. 2013; Morgenstern et al. 2017; WMO 2011). Here, the RCP6.0 scenario assumes an increase of 6 W m^{-2} in the global radiative forcing by the end of the twenty-first century compared to the preindustrial period (Taylor et al. 2012). We follow the naming convention by Morgenstern et al. (2017) for the CCMI-1 models and refer to this study for a comprehensive description of each model's individual setup.

In addition, we compare five models that are part of CMIP6 (Eyring et al. 2016) and that include interactive chemistry schemes [cf. Table 1, following the assessment by Keeble et al. (2021)]. Here, we limit our analysis to the CMIP6 shared socioeconomic pathway (SSP) 2-4.5 and SSP5-8.5 projections, which simulate an increase of 4.5 and 8.5 W m^{-2} in the radiative forcing by 2100, respectively, and additionally, each includes the global impacts of a possible SSP, that is, SSP2 (usually entitled as the "Middle of the road" scenario in the existing literature) and SSP5 ("Fossil-fueled development"), respectively (O'Neill et al. 2016; Riahi et al. 2017; Meinshausen et al. 2020). We use each model's first three ensemble runs, except for GFDL-ESM4 and MRI-ESM2.0 where at the time of this analysis the required model data were provided only for one ensemble member. For CESM2 (WACCM), no total-column ozone data were available.

We consider the CCMI-1 (CMIP6) data on 27 (19) pressure levels between 1 and 1000 hPa, which we interpolated on a meridional grid with 2.5° resolution. MOCAGE and UMSLIMCAT only provided output below 10 hPa and above 250 hPa, respectively. We furthermore limit the time range of our analysis to maximize the number of models for which the corresponding data are available, i.e., 1979–2008 for CCMI-1 REF-C1 and 2015–98 for CCMI-1 REF-C2 and the CMIP6 projections. We use ensemble-mean data for each individual model if more than one run is available (cf. Table 1).

b. *Jet stream variability*

In this work, we consider the year-by-year variability of the STJ in both hemispheres by assessing changes in the magnitude and the meridional location of zonal-mean maximum zonal wind speeds in the STJ regions. We follow the method by Davis and Birner (2013, 2017) and consider the maximum zonal wind vertical shear (relative to the 850-hPa zonal wind) as a function of latitude, where only data points up to 50 hPa above the thermal tropopause are included. The hemispheric maximum of this meridional profile of zonal wind shear maxima defines the strength of the STJ (STJ MAX), and the STJ's latitudinal position (STJ LAT) is obtained from the zero crossing of the associated meridional derivative profile (Davis and Birner 2013, 2017). To link our results to previous work and explore linkages between the STJ and the EDJ stream, we also diagnose the EDJ. In particular, we define the EDJ's magnitude (EDJ MAX) as the maximum of the zonal-mean zonal wind at 850 hPa, with EDJ's meridional location (EDJ LAT). Table 2 provides an overview of the jet stream metrics considered in this study.

Previous studies also referred to the STJ as an indicator of tropical circulation changes, in particular of variations in the meridional extent of the overturning Hadley cell (e.g., Davis and Birner 2017; Staten et al. 2018; Waugh et al. 2018). Here,

TABLE 2. Overview of jet stream diagnostics used in this analysis.

Label	Description
STJ MAX	Maximum strength of the vertical shear of the zonal-mean zonal wind between 850 hPa and any given higher level; altitudes higher than 50 hPa above the thermal tropopause are excluded in the data (Davis and Birner 2013, 2017)
STJ LAT	Following Davis and Birner (2013, 2017), latitude of STJ MAX, derived from the zero crossing of the meridional derivative profile of maximum zonal wind vertical shear as a function of latitude
EDJ LAT	Latitude of maximum zonal-mean zonal wind at 850 hPa in the midlatitudes (e.g., Waugh et al. 2018; Adam et al. 2018a)
EDJ MAX	Zonal-mean zonal wind interpolated at EDJ LAT

in the interest of clarity, we will limit our analysis to the correspondence between (direct) wind field–related and (indirect) ozone-based metrics of STJ and EDJ variability. In some cases, we will point to extended results that are provided in the supplemental material.

In general, we quantify statistical jet stream covariability by computing Pearson correlation coefficients, where the linear trends of the anomaly time series, as obtained from least squares linear regressions, are removed beforehand. The correlation coefficients' confidence intervals are calculated using Fisher's z transformation. Similarly, we derive regression maps in the latitude–height plane pointwise by regressing the anomaly time series of the given data field (the predictand) at each grid point on a one-dimensional predictor index, after subtracting linear trends.

For calculating the jet stream diagnostics described above and tropical width metrics, we partially make use of "PyTropD" (Ming 2022), which is the Python edition of the "Tropical-Width Diagnostics" ("TropD") software developed by Adam et al. (2018a,b). We also use various helper functions that are available from PyTropD. Furthermore, if not stated otherwise, we refer to the WMO (1957) thermal tropopause in this paper, which we calculate from a modified version of PyTropD's internal routine `TropD_Calculate_TropopauseHeight`. The modification was necessary because the implemented criterion for the lapse rate tropopause definition in PyTropD turned out to be too strong.

3. Definition of ozone gradient diagnostics

The ozone metrics proposed in this work aim to detect STJ changes by measuring the variations of monthly mean, zonal-mean ozone near the STJ in each hemisphere. The climatological ozone distribution features well-pronounced gradients in the UTLS region (cf. Fig. 1) where the tropopause and the STJ act as tracer transport barriers. This motivates the different ozone gradient definitions discussed in this section, which are also listed in Table 3. We probe three different methods for diagnosing proxies of the STJ based on the meridional ozone gradients. Two of them require vertically resolved ozone data, while the third approach uses TCO profiles, which may be useful for application due to the availability of long-term TCO observational records (cf. section 5b). Two additional methods testing minor modifications of the setup are shown in the supplemental material.

The first diagnostic in Table 3 is based on the field of the meridional ozone gradient with respect to geographical latitude ϕ:

$$\mathrm{O3GRAD}(t, p, \phi) \equiv \frac{\partial_\phi \overline{\chi}}{\langle \overline{\chi} \rangle_t}, \tag{1}$$

which is derived from the ozone distribution in the latitude–pressure plane $\overline{\chi}(t, p, \phi)$, where the overbars in our notation denote zonal-mean quantities. The gradient field is weighted by the zonal-mean ozone climatology $\langle \overline{\chi} \rangle_t \equiv \langle \overline{\chi}(t, p, \phi) \rangle_t$, such that O3GRAD provides a relative measure of changes in zonal-mean ozone and therefore is insensitive to the background ozone mixing ratios that usually vary strongly with altitude.

The isolines of zonal-mean ozone in the UTLS closely follow the tropopause, in particular the tropopause break in the STJ region is closely aligned with a strong slope in ozone isolines (see Fig. 1b). This motivates to use a second metric that is derived from the meridional gradients of the height of

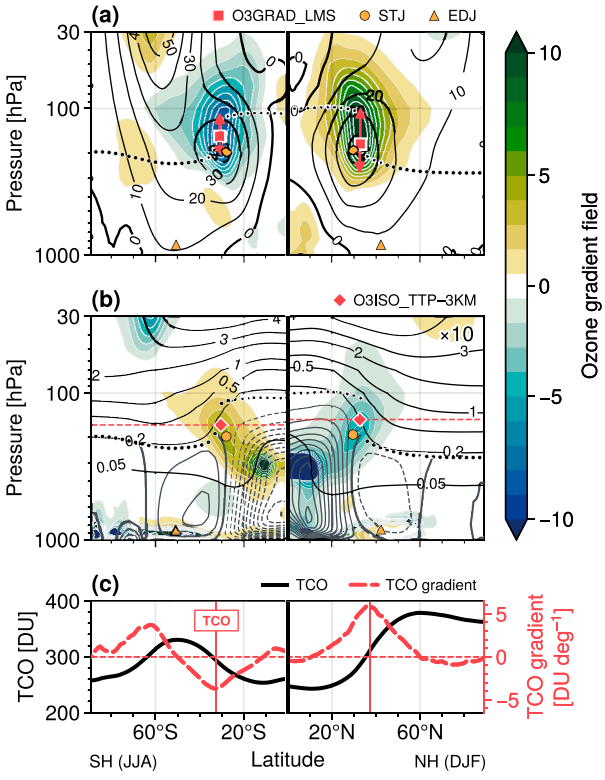

FIG. 1. Overview of the different ozone diagnostics and the underlying ozone gradient fields considered in this work. All panels show winter-mean climatologies derived from ERA5 reanalysis data 1979–2023 (NH DJF and SH JJA, respectively). The color codings provide (a) the meridional ozone gradient field (% deg^{-1}) and (b) the ozone isoline gradient field (km deg^{-1}, scaled by a factor of 10), both computed from winter-mean climatological ozone. Contour lines show (a) the zonal-mean zonal wind (m s^{-1}) and (b) the zonal-mean ozone distribution (ppmv, black contours) as well as the mean meridional mass streamfunction [gray contour lines with intervals of 2×10^{10} kg s^{-1}, displayed below the tropopause only; computed using PyTropD by Adam et al. (2018a)]. The thick dotted lines in (a) and (b) show the mean thermal tropopause. The orange and red markers in (a) and (b) show the meridional locations of the jet stream cores and ozone gradient maxima, respectively. In (a), red vertical arrows illustrate the altitude range for vertical averaging of the ozone gradient profiles, as defined for the O3GRAD_LMS metric in Table 3. The reference level Z_{ref} for the O3ISO_TTP–3KM diagnostic in (b) is marked by the red dashed lines. (c) Winter-mean TCO in Dobson units (DUs; solid lines) and the corresponding meridional gradient profile (DU deg^{-1}, dashed lines), with the locations of the subtropical gradient maxima indicated by vertical red lines.

TABLE 3. Classification of ozone gradient metrics. See the main text for a detailed description.

Label	Gradient (unit)	Required data	Profile	Definition[a]
O3GRAD_LMS	Meridional (% °N^{-1})	Vertically resolved ozone field	Vertical averaging with $N = 10$ levels	$\sum_{i=0}^{N-1} \mathrm{O3GRAD}[t, Z = Z_{\mathrm{TTP}}(t) + i\delta Z, \phi]/N$ with $\delta Z = [Z_{\mathrm{PTP}}(t) - Z_{\mathrm{TTP}}(t)]/(N-1)$
O3ISO_TTP–3KM	Isoline (km °N^{-1})	Vertically resolved ozone field	3 km below tropical tropopause height	$\mathrm{O3ISO}[t, p = p_{\mathrm{ref}}(t), \phi]$
TCO	Meridional (DU °N^{-1})[b]	TCO	—	$\partial_\phi \mathrm{TCO}(t, \phi)$

[a]Definitions of O3GRAD and O3ISO as in Eqs. (1) and (2) in the main text, respectively.
[b]DU = Dobson unit.

zonal-mean ozone isolines (referred to as "ozone isoline gradient field" in the following):

$$\mathrm{O3ISO}(t, p, \phi) \equiv \left.\frac{dZ(p)}{d\phi}\right|_{\overline{\chi}=\text{const.}} = -\frac{\partial_\phi \overline{\chi}}{\partial_Z \overline{\chi}}(t, Z, \phi) = \frac{H}{p}\frac{\partial_\phi \overline{\chi}}{\partial_p \overline{\chi}}(t, p, \phi), \quad (2)$$

where $Z(p) \equiv H\log(p_0/p)$ denotes log-pressure height with scale height $H = 7$ km and surface pressure $p_0 = 1000$ hPa.

Figure 1 provides the winter-mean climatologies of these ozone gradient fields computed from monthly mean ERA5 reanalysis data for 1979–2023 [Northern Hemisphere (NH) DJF and Southern Hemisphere (SH) JJA]. The meridional ozone gradient field in Fig. 1a clearly shows one subtropical extremum in each hemisphere. These extrema are vertically stretched, roughly following the tropopause break, and peak around the STJ core. The ozone isoline gradient field peaks in the tropics around 300 hPa, expanding across the tropopause break into the lowermost stratosphere (Fig. 1b). Here, the high tropospheric gradients correspond to steep isoline curvatures, which are formed by both up- and downward ozone transport through the overturning Hadley circulation in the tropics (illustrated by the $\overline{\chi} = 50$ ppbv ozone isoline and the mean meridional mass streamfunction in Fig. 1b).

Except for the TCO gradient metric, it is necessary to apply vertical averaging or level selection to gain latitudinal profiles from the two-dimensional gradient fields, which the metric can be based upon. We tested different procedures to perform the vertical selection (see also supplemental material) and settled on the following:

1) Due to the vertically coherent structure of the subtropical O3GRAD extrema (Fig. 1a), we average vertically across $N = 10$ equidistant log-pressure height levels, equally distributed between the mean tropical tropopause (TTP; $\phi < 20°$) and the mean polar tropopause (PTP; $\phi > 60°$). To capture vertical shifts and fluctuations of the lowermost stratosphere (LMS) over time, we allow both TTP and PTP to be a function of time (at monthly resolution as with other diagnostics). We refer to the resulting ozone gradient metric as "O3GRAD_LMS" (cf. Table 3).
2) We select fixed reference levels $Z_{\mathrm{ref}} = H\log(p_0/p_{\mathrm{ref}})$ onto which the ozone isoline gradient field (O3ISO) is interpolated (cf. Fig. 1b). Again, to account for vertical shifts and fluctuations, this level is adapted monthly. Here, we link this reference level to the mean tropical tropopause height, i.e.,

$$Z_{\mathrm{ref}}(t) \equiv Z_{\mathrm{TTP}}(t) + \Delta Z, \quad (3)$$

where ΔZ denotes a constant offset. We set $\Delta Z = -3$ km in the following, representing an isobar that is located below the TTP and that approaches the altitude of the STJ core to maximize STJ covariability. Note, however, that biases in observational ozone data due to measurement limitations occur especially at lower altitudes (cf. section 5), which effectively narrows the range of suitable offset values ΔZ. The corresponding metric is called "O3ISO_TTP–3KM" in Table 3 and aims to track changes associated with STJ dynamics across the set of isolines featuring strong curvatures along the tropopause break.

Figure 1 shows that all these ozone gradient definitions, O3GRAD_LMS, O3ISO_TTP–3KM, and TCO, feature well-pronounced subtropical extrema for both hemispheres on a climatological average. As a final step, we derive two types of key parameters for each profile. Given multiple time steps, they form two index time series:

- The *absolute* magnitude of the subtropical extremum, searched for among all data points across latitude and for each month and each hemisphere separately, referred to by adding a suffix "MAX" behind each definition's label. Accordingly, accounting for the sign convention in our gradient definitions, from now on we will always refer to absolute subtropical gradient *maxima* for both hemispheres.
- The latitude of that maximum, applying the smoothing approach with strength parameter $n = 6$ introduced by Adam et al. (2018a), where we use PyTropD's `TropD_Calculate_MaxLat` routine, labeled by adding a suffix "LAT."

The climatological location (LAT) of each ozone gradient maximum is illustrated in Fig. 1. During our analysis, we found substantial differences in the gradient maxima's average strength throughout the year due to the seasonal cycle. In the appendix, we provide a qualitative estimate on their variable peak sharpness, which turned out to be significantly reduced especially during summer, causing issues in identifying these maxima. We therefore limit our analysis to hemispheric winters in the following and add the results for annual-mean data where appropriate to allow for a comparison with the results from the existing literature.

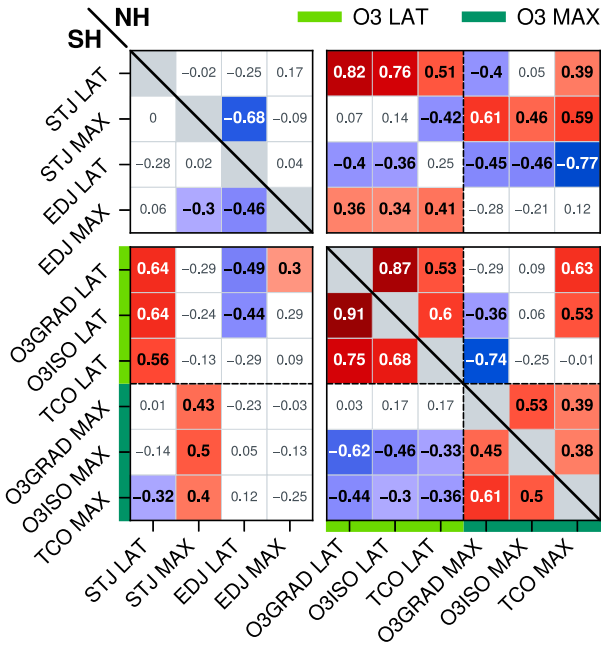

FIG. 2. Pearson's correlation coefficients, based on interannual variability, for all combinations of detrended jet stream and gradient-based ozone diagnostics listed in Tables 2 and 3, respectively. The results were computed separately for the NH (upper-right area) and SH (lower-left area), based on winter-mean ERA5 data (1979–2023, NH DJF, and SH JJA). For better readability, the ozone gradient diagnostics are divided into two groups of "O3 LAT" and "O3 MAX" time series, which are marked by the light and dark green panel shading, respectively. In addition, the O3GRAD_LMS metric from Table 3 here is abbreviated as "O3GRAD" and similar for O3ISO_TTP–3KM which is denoted as "O3ISO." Statistical significance at the 95% level was found where color coding and bold type are applied to the corresponding entries in this table. Plot design inspired by Waugh et al. (2018, their Fig. 5).

4. Ozone gradient metrics in ERA5 reanalyses

In this section, we evaluate the statistical relation of interannual variability between the jet stream diagnostics from Table 2 and the ozone gradient metrics defined in Table 3 and try to shed light on the physical mechanism behind their correspondence.

Figure 2 provides the associated correlation coefficients based on winter-mean ERA5 reanalysis data for 1979–2023, combining the results for the NH and SH (based on DJF and JJA winter seasons, respectively). Here, the individual entries in the correlation table are color coded if the statistical significance of the associated correlation was found at the 95% level. We note that, overall, the different ozone gradient definitions mostly agree well in measuring interannual variations in the location and strength of the subtropical gradient maxima, as indicated by the strong correlations within the two sets of LAT and MAX ozone indices, respectively (lower-right panel of Fig. 2). In particular, we find the most robust correlations among the LAT-type metrics ("O3 LAT") in both hemispheres. In the NH, TCO MAX is significantly coupled with the LAT time series of the two other ozone gradient metrics, and TCO LAT is strongly anticorrelated with the O3_GRAD_LMS maxima. TCO LAT and TCO MAX themselves, however, turn out to be decoupled and similar for the LAT and MAX of the O3GRAD_LMS and O3ISO_TTP–3KM diagnostics, indicating that they represent distinct variability modes. In the SH, this only holds for the O3GRAD_LMS definition, and we find significant anticorrelations among the LAT and MAX metrics based on TCO and isoline gradients.

Across all ozone-based metrics, we find robust correlations with the STJ properties; i.e., the latitudinal positions of the ozone gradients (O3 LAT class of indices) vary with the STJ latitude and are similar for the gradients' magnitudes (O3 MAX) and the strength of the STJ in both hemispheres (lower-left and upper-right panels in Fig. 2). This relation is strongest between STJ LAT and the LAT-type gradient metrics in the NH. Here, we also find substantial anticorrelations between the MAX-type metrics and the EDJ LAT, which is likely due to the dynamical coupling between EDJ LAT and the strength of the STJ ($r = -0.68$ for NH in the upper-left panel of Fig. 2). Similarly, EDJ MAX is robustly coupled with the O3 LAT time series in the NH, although STJ LAT and EDJ MAX are not directly linked in ERA5 ($r = 0.17$).

Overall, we find high consistency between ozone-based metrics of the strength and latitude of the subtropical maximum and a high correlation to the respective STJ properties. An extended version of Fig. 2 is provided as Fig. S1 in the online supplemental material, showing also correlations between two slightly modified versions of the above introduced ozone gradient diagnostics, as well as common metrics of tropical width associated with the tropospheric meridional mass streamfunction, the subtropical tropopause break, and near-surface zonal winds.

For understanding the covariability with the STJ, consider Fig. 3 which shows the responses of the underlying ozone gradients to variations of STJ strength and position. These are computed by regressing the winter-mean ozone gradient anomalies on the standardized index time series STJ MAX and STJ LAT, respectively (ERA5, 1979–2023, NH DJF, and SH JJA). In addition, we consider the meridional gradient field of modified potential vorticity (Lait 1994):

$$\partial_\phi \overline{\Pi} \equiv \partial_\phi [\overline{P}(\overline{\theta}/\theta_0)^{-9/2}], \tag{4}$$

where $\overline{P}$ denotes the zonal-mean potential vorticity (PV) and $\overline{\theta}$ is the zonal-mean potential temperature with reference level $\theta_0 \equiv 300$ K. We find that the subtropical gradient maxima in the O3GRAD, O3ISO, and PV fields simultaneously follow the changes in the latitudinal position of the STJ, as indicated by the dipole-like response signatures in Figs. 3a–c. Likewise, in all cases, we clearly observe sharper gradients when the STJ strengthens (Figs. 3e–g). This is consistent with the meridional PV gradient acting as a tracer transport barrier in the STJ region, regulating the amount and the equatorward extent of quasi-isentropic ozone transport by eddy mixing across the subtropical tropopause. Figure 3 also shows that

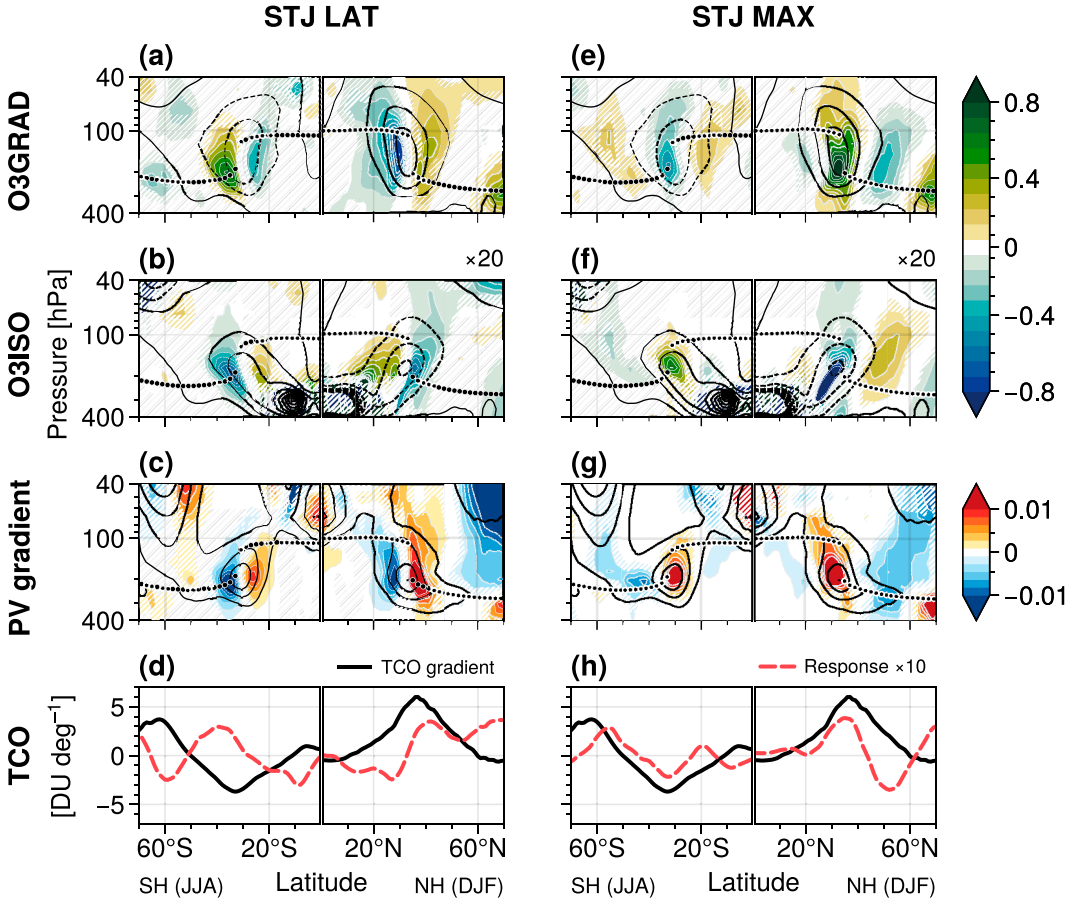

FIG. 3. Meridional ozone gradient field (O3GRAD), ozone isoline gradient field (O3ISO, scaled by an additional factor of 20 for plotting), and meridional gradient field of modified PV (Lait 1994) regressed on the standardized (a)–(c) STJ LAT and (e)–(g) STJ MAX index time series, respectively. The regression maps are shown in units of percent per degree (% deg^{-1}), kilometers per degree (km deg^{-1}), and PV units per degree (PVU deg^{-1}), respectively, per standard deviation of the STJ predictors. Black contours show the structures of the gradient field climatologies (dashed lines indicate negative values). The thick dotted lines represent the mean thermal tropopause. (d),(h) As before, but for the response (red dashed lines) of the TCO meridional gradient profiles (DU deg^{-1}; black lines show climatology), obtained by linear regression on the standardized STJ diagnostics. All results were calculated from winter-mean ERA5 reanalysis data (1979–2023). Hatches indicate where the regression maps are not statistically significant at the 95% level.

the response signals in the SH are less pronounced and more confined to narrow altitude ranges compared to the NH, which may be associated with the weaker correlation coefficients during austral winter found in Fig. 2 (lower-left panel). We hypothesize that the limited contribution of planetary-scale atmospheric waves in the SH may play a role here, but analyzing the local ozone budget as a function of zonal wavenumber is left for future work. Note that the regression maps in Fig. 3 show the response relative to the ozone gradient climatology (illustrated by the black contour lines), which partially feature subtropical gradient *minima* (i.e., negative meridional gradients). However, the associated correlation coefficients are always positive in Fig. 2 as we consider *absolute* gradient magnitudes.

In addition, Figs. 3d and 3h provide further evidence that STJ covariability is also reflected by the meridional TCO gradients similar to the vertically resolved ozone gradients but with some deviations from the simple response signatures characterizing the shifting and strengthening of the gradient maxima upon changes in STJ LAT and STJ MAX, respectively. These differences are consistent with the significant amount of cross correlations with the TCO metrics identified in Fig. 2. Note that especially in the NH, we also expect some impact on tropospheric ozone due to meridional fluctuations of the midlatitude jet (EDJ LAT) where we found a strong anticorrelation with the TCO MAX diagnostic $r = -0.77$ according to Fig. 2.

The results from this section show that the gradient-based ozone metrics primarily measure variations of the STJ, which appeared to be consistent with our knowledge on the jet working as a dynamically fluctuating ozone transport barrier in the subtropics. We found a clear dichotomous behavior

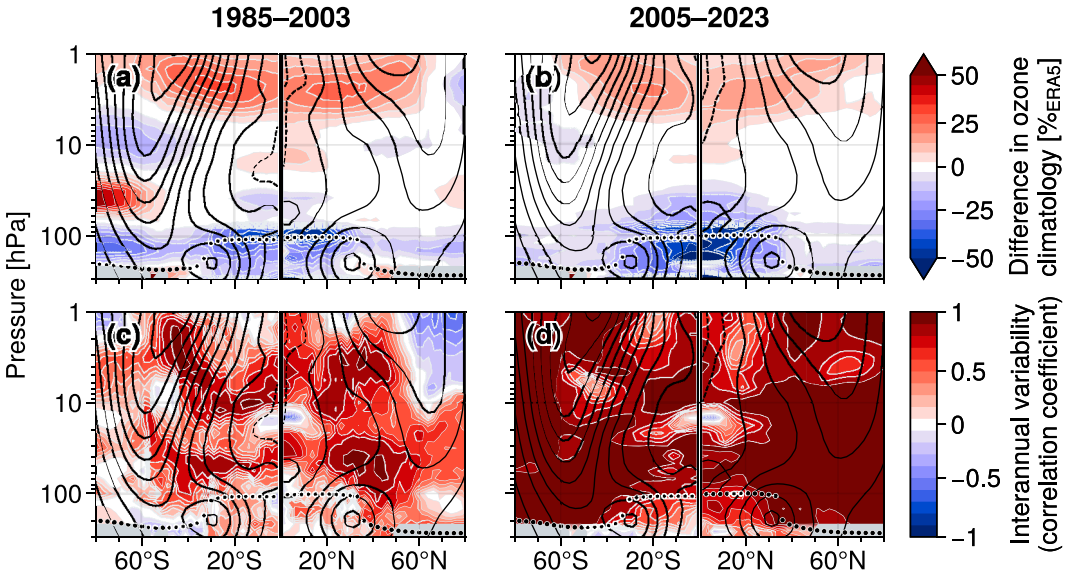

FIG. 4. (a),(b) Differences in climatological zonal-mean ozone during winter (NH DJF and SH JJA) between ERA5 and SWOOSH relative to ERA5 ozone. (c),(d) Correlation coefficients for interannual zonal-mean ozone variability derived from SWOOSH compared to ERA5. Contour lines show the corresponding zonal-mean zonal wind climatologies. The thick dotted lines illustrate the winter-mean tropopause. The left and right columns of this figure provide the results for the time periods until 2003 and starting 2005, respectively.

among these ozone metrics, i.e., statistically significant correspondence of the index time series with either the varying zonal-mean zonal wind strength in the STJ region (subset of MAX-type indices) or with the jet's meridional position (LAT). In the NH, the metrics measuring fluctuations in the strength (or meridional position) of the STJ are also coupled to the shifting (or strengthening) of the EDJ (cf. Lorenz and Hartmann 2001, 2003).

5. Comparison with observational data

After constructing tracer-based diagnostics for STJ variability, we now make use of observational records in two ways: First, we evaluate the ozone index time series obtained from ERA5 reanalysis data by comparing them with ozone measurements. Second, we derive trends across the historical time period and evaluate the trend uncertainties of this observation-based approach.

a. Comparison with SWOOSH ozone data

We use the SWOOSH dataset described in section 2 to evaluate the ozone gradient definitions from Table 3 that are based on the vertically resolved distribution of zonal-mean ozone. As indicated by Figs. 4a and 4b, especially in the middle stratosphere, winter-mean ERA5 ozone agrees well with SWOOSH ozone across two predefined time intervals of equal length ranging 1985–2003 and 2005–23, respectively. The biases in the climatological ozone distribution mainly occur in the tropical UTLS region and in the upper stratosphere. We find substantial differences in ERA5 and SWOOSH interannual ozone covariability between these two time intervals, as measured by pointwise Pearson correlation coefficients in the latitude–pressure plane: Figs. 4c and 4d show a less homogeneous and rather modest correlation between ERA5 and SWOOSH year-by-year ozone anomalies prior to 2005 and strongly increased correlation values across almost the entire meridional plane after that date. This is presumably due to the availability of global, densely sampled Aura MLS measurements (Waters et al. 2006), which entered both the SWOOSH data processing and ERA5 data assimilation in more recent years. Overall, although differences between ERA5 and SWOOSH ozone are still substantial for 2005–23 around the STJ in both hemispheres, winter-mean ozone anomalies, which play a key role in defining ozone-based metrics of atmospheric variability, seem to agree much better in more recent years (as seen by the high correlation values in Fig. 4d).

Intercomparisons between the ERA5 and SWOOSH ozone gradient metrics turned out to be challenging due to the substantial differences in interannual ozone variability between the earlier and later parts of the available time period. In particular, artifacts in the SWOOSH ozone gradient profiles prior to 2005 resulting from missing and noisy data in the UTLS caused problems when applying our computation routines (not shown). During this time period, SWOOSH is dominated by data from solar occultation sensors that provide around two orders of magnitude less data than Aura MLS and are subject to cloud and aerosol interference (e.g., due to Mount Pinatubo) that results in very sparse sampling in the UTLS. As a consequence, we found poor correlations between the ERA5 and SWOOSH ozone metrics for the time period up to 2005 and mostly very good agreement for the recent years

(not shown). The O3ISO_TTP–3KM definition represents the only exception with no statistically significant correlations during 2005–23. This is probably due to the underlying isoline height gradient fields, which are based on both meridional and vertical ozone gradients [cf. Eq. (2)] and therefore may be much more sensitive to biases in the ERA5 and SWOOSH ozone data. We obtained much better agreement between the ERA5 and SWOOSH O3ISO metrics when we shifted the reference level Z_{ref} for evaluating the gradient profiles upward (not shown), i.e., if ΔZ was increased in Eq. (3). This is because the relative differences between the reanalysis data and the ozone measurements decrease at higher altitudes. However, we found that modification of ΔZ can also lead to reduced covariability of the ozone gradient metrics with the STJ, indicating an important trade-off in the parameter setup.

b. *Historical trends from TCO observations*

Our analysis showed that observational, vertically resolved ozone data are not yet available in sufficient quality and for a long enough time period to allow an assessment of trends based on the two-dimensional, zonal-mean ozone gradient fields O3GRAD and O3ISO. We therefore apply the two total-column ozone gradient metrics, TCO LAT and TCO MAX, where we compare TCO from ERA5 and the ESA CCI MSR. Since the underlying model for the ESA MSR uses ECMWF meteorological data (Van Roozendael et al. 2021a), we examine zonal-mean "BS Filled" TCO data by Bodeker et al. (2021) as an additional, and perhaps more independent, reference. Using these datasets, we compare historical trends in the TCO-based metrics with the trends found in the strength and location of the jet streams, which we derive directly from global zonal-mean zonal wind data from the ERA5, CFSR/CFSv2, JRA-3Q, and MERRA-2 reanalyses (S-RIP RID; Martineau et al. 2018). It is not clear a priori whether and how variations in TCO, indicating variability of vertically accumulated ozone, allow for a precise quantification of local covariability between the jet stream and ozone in the STJ regions. The TCO gradient metrics may still represent indirect but meaningful indicators of jet stream variability if they are sufficiently well related to the jet stream properties under consideration, i.e., significant correlations between these TCO-based diagnostics and the STJ are essential for the subsequent interpretation of the results.

Figure 5 provides the results for the years 1980–2019, where we computed linear trends from annually resolved data based on both winter-mean and annual-mean anomalies and for both hemispheres separately. Here, we estimated the trend uncertainties from a bootstrapping approach, each based on 1000 randomly sampled time series containing 30 out of the 40 index time steps. All reanalyses indicate a poleward movement of the STJ in both hemispheres and for both winter mean and annual mean (Figs. 5a,d,g,j), albeit not all of these trends are statistically significant. However, the high correlations and mostly similar trend magnitudes across these four reanalyses suggest that these trends may be robust. We find that, if the correlation with STJ LAT is significantly strong (i.e., as given in Figs. 5a,d,g but not Fig. 5j, as indicated by the colored boxes at the bottom of each panel), then indeed the TCO LAT metric qualitatively reproduces this poleward shifting of the STJ for all three TCO datasets (ERA5, MSR, and BS; red bars in Fig. 5). We find larger trends in the TCO metrics than for the STJ, which is consistent with stronger interannual variability in TCO LAT compared to STJ LAT (not shown). This may be due to chemical and nonlinear effects and due to advective ozone transport beyond the STJ core, which is not governed by the strength of the subtropical mixing barriers. In general, based on the TCO LAT trend $\Delta\phi_{\mathrm{TCO}}$, the trend in jet latitude may be indirectly estimated from TCO covariability as

$$\Delta\phi_{\mathrm{STJ}} \simeq b[\mathrm{TCO}, \mathrm{STJ}] \cdot \Delta\phi_{\mathrm{TCO}}, \tag{5}$$

where b[TCO, STJ] is the linear regression coefficient of the multireanalysis STJ anomaly time series regressed on the TCO index. This indirect estimate assumes that the system dynamics giving rise to the trend behave the same as those giving rise to intrinsic, interannual variability. This is somewhat akin to the fluctuation–dissipation theorem (e.g., Leith 1975). We find that the magnitudes of poleward STJ movement inferred from the TCO scale well with the direct reanalysis STJ LAT trends for winter-mean NH variability (orange bars in Fig. 5a) but are substantially reduced for the SH compared to the wind field–related STJ metric in Fig. 5g. In contrast, enhanced trend values are found for NH annual-mean data, where now the TCO trends show statistical significance, whereas STJ LAT trends from the reanalysis data do not (Fig. 5d).

For the NH during winter, Figs. 5b and 5c furthermore show that the trends in the STJ's strength (STJ MAX) and the location of the midlatitude jet (EDJ LAT) are not statistically significant, and neither are the trends in TCO MAX. For annual-mean data, TCO MAX trends suggest a robust weakening of the STJ and a poleward shift of the EDJ during the historical time period, which qualitatively agrees with the (nonsignificant) STJ MAX and EDJ LAT reanalysis trends (Figs. 5e,f). In particular, Fig. 5e provides an example where the statistically significant trend estimates from the observation-based TCO MAX metric may help to constrain the diverging results on STJ MAX trends from the different reanalyses.

Finally, Figs. 5g–l suggest that constraining jet variability from our TCO gradient metrics is rather challenging in the SH. In particular, the TCO LAT trend magnitudes in Fig. 5g roughly compare with the NH results (Fig. 5a), but we find much larger confidence intervals, presumably due to the limited availability of observational data during Austral winter and weaker TCO gradients in the subtropics compared to the NH. Further conclusions, e.g., on covariability with STJ MAX and EDJ LAT in the SH, turn out to be difficult due to the insufficient statistical correlations with the TCO diagnostics (cf. white boxes indicating weak correlations in Figs. 5h,i). Finally, the statistically significant annual-mean TCO MAX trends suggest poleward movement of the EDJ (orange bars in Fig. 5l) and weakening of the STJ (orange bars in Fig. 5k), but the latter contradicts the robust STJ MAX trends from the

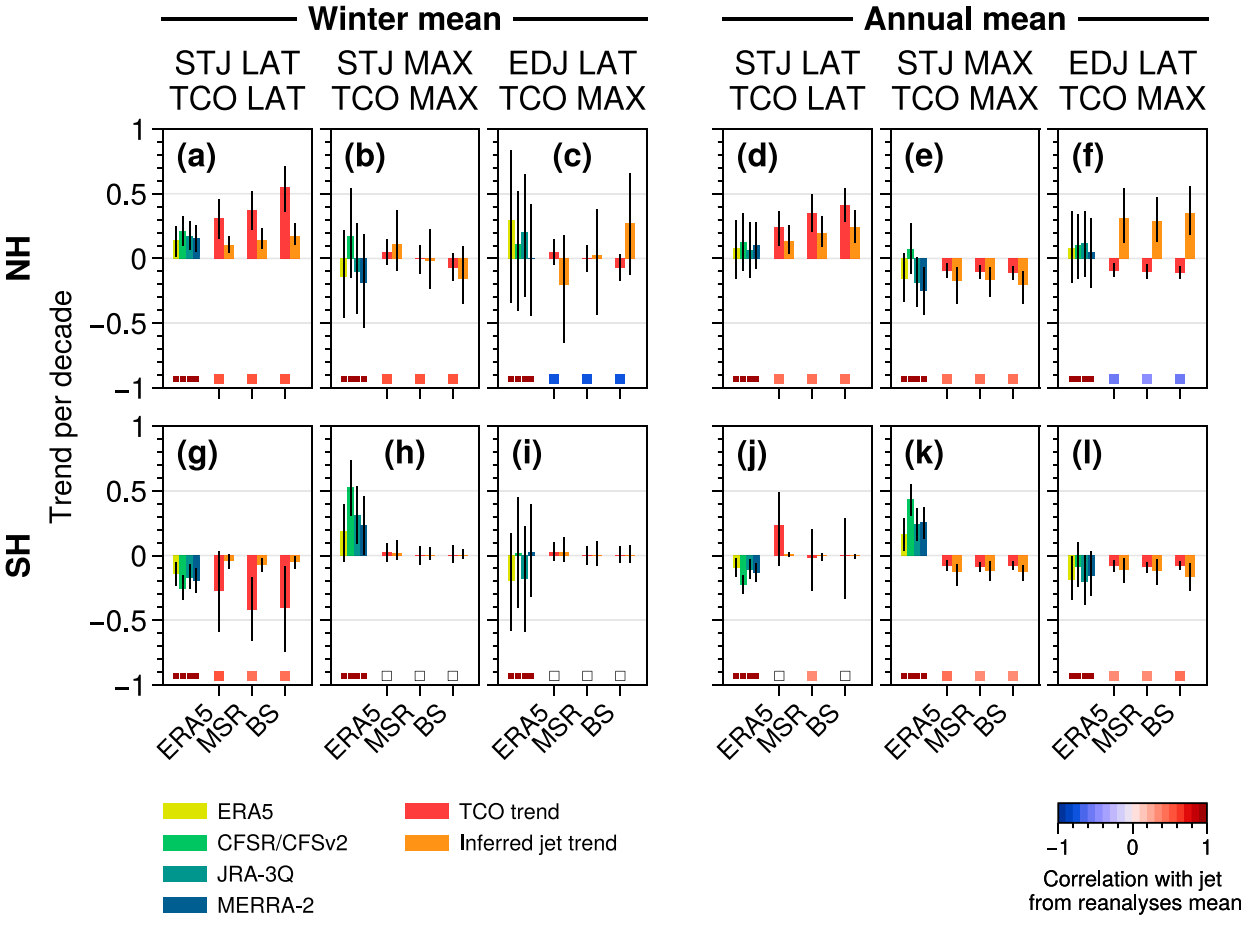

FIG. 5. Historical (1980–2019) STJ and EDJ trends from reanalyses (green bars on the left side of each panel) and TCO trends (red bars) from ERA5, MSR, and BS TCO data. TCO trends are compared to the TCO LAT time series for STJ LAT, and TCO MAX otherwise, following the correlation table in Fig. 2. The unit of all LAT trends is degrees per decade (deg decade^{-1}), where positive values indicate a northward shift. STJ MAX and TCO MAX trends are provided in units of m s^{-1} decade^{-1} and DU deg^{-1} decade^{-1}, respectively. Correlation coefficients with the multireanalysis mean jet variability are provided by the color-coded boxes at the lower end of each panel, where white boxes indicate that no significant correlation was found at the 95% level. The orange bars provide estimates on the jet trend magnitudes obtained from TCO variability according to Eq. (5). Error bars provide 95% confidence intervals derived from a bootstrapping approach each based on 1000 randomly sampled 30-yr time series.

reanalyses. Note that in Figs. 5k and 5l, correlations between TCO MAX and the two jet stream metrics are statistically significant but rather weak, which complicates interpretations. In addition, substantial ozone depletion in the SH higher latitudes may impact the subtropical TCO gradients, which may weaken the relation between jet stream variability and ozone gradient changes.

6. Ozone gradient metrics from climate simulations

In this section, we first assess how the relation between jet stream variability and ozone gradients is represented in CCMI-1 climate models as compared to ERA5 reanalysis data. Figure 6 shows the multimodel averaged correlation coefficients similar to the ERA5 correlations shown in Fig. 2, where we used winter-mean 1979–2008 model output from 17 CCMI-1 REF-C1 hindcast simulations listed in Table 1. The corresponding correlation table for each individual model is available in the supplemental material. Statistical robustness is assumed where at least 80% of the models agree on the sign of covariability and provide a statistically significant correlation at the 95% level (indicated by colors). Additionally, agreement in terms of the spread of the correlations between models, as measured by cross-model standard deviations, is indicated by bold numbers as an indication of robustness, in the case of significant correlations with a threshold of 25% of the multimodel mean (MMM) and 50% for the nonsignificant correlation values.

Figure 6 (lower-right panel) shows that the CCMI models provide some robust correlations within the two groups of O3 MAX and O3 LAT ozone metrics, respectively, which is mostly consistent with ERA5 except for the correlations related to TCO LAT where the models simulate weaker correlations. Furthermore, the models do not reproduce the ERA5

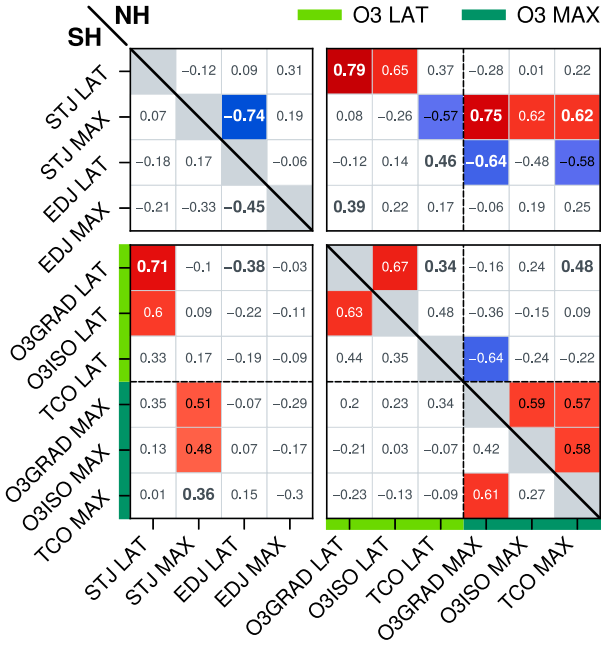

FIG. 6. Table of correlation coefficients for winter-mean jet stream and ozone gradient metrics obtained from 17 CCMI-1 REF-C1 hindcast simulations listed in Table 1 (1979–2008). The color coding provides an estimate on the statistical robustness of each correlation; i.e., at least 80% of the models agree on the sign of the correlation coefficient and show statistical significance at the 95% level. Bold type numbers indicate that the cross-model standard deviation of the correlations is below 25% (50%) of the MMM for the (non)significant correlation values. Other details are as in Fig. 2.

anticorrelations between O3 MAX and O3 LAT metrics in the SH, and the substantial model spreads there (>50% according to the formatting criterion described above) suggest that the strength of this coupling is influenced by the different modeling schemes. In contrast, the robust anticorrelation between O3GRAD_LMS MAX and TCO LAT in the NH agrees quite well with ERA5. Overall, the CCMI models clearly reflect the two-mode behavior of the ozone gradient diagnostics, where we found that O3 LAT metrics strongly correlate with the STJ's meridional position (STJ LAT) in both hemispheres and are similar for O3 MAX and STJ MAX (lower-left and upper-right panels in Fig. 6). Substantially reduced correlations are only found for TCO LAT. In some cases, the high correlation magnitudes and reduced model spreads provide evidence that STJ–ozone covariability in part is even more pronounced than in ERA5 (cf. individual models in the supplemental material). We hypothesize that the inconsistencies in the reanalysis output due to data assimilation may play a role here. The simulations also reproduce the significant anticorrelation between the strength of the STJ (STJ MAX) and the EDJ LAT in the NH ($r = -0.74$, upper-left panel in Fig. 6) and, as a consequence, robust anticorrelations between O3 MAX metrics and EDJ LAT.

As a second step, we analyze the projected trends for the twenty-first century in the zonal-mean ozone gradient structure in the subtropics, in particular associated with variations in the strength and location of the STJ in both hemispheres. To do so, we use monthly averaged model output from the CCMI-1 REF-C2 climate projections (17 models; cf. Table 1). We compare them with simulations from the CMIP6 using two different SSP climate forcing scenarios, where we select five CMIP6 models that use an interactive chemistry scheme [following Keeble et al. (2021)]. Figure 7 provides the linear trends found in the STJ metrics and in the ozone gradient time series defined in Table 3, as obtained from winter-mean projections for the years 2015–98.

Figures 7b and 7d show that the O3GRAD_LMS MAX and TCO MAX time series feature positive multimodel mean trends (illustrated by the vertical bars) for all three scenarios (REF-C2, SSP2-4.5, and SSP5-8.5), indicating a strengthening of the meridional ozone gradients in the STJ region in both hemispheres. This is consistent with the projected increase in STJ zonal wind speeds, which act to strengthen the effective dynamical transport barrier for wave-induced ozone mixing. For O3ISO_TTP–3KM, we find similar results except for CCMI-1 REF-C2 where some model outliers cause rather extreme multimodel mean trends.

Direct comparison of the CCMI-1 and CMIP6 groups of simulations needs to be treated with caution due to the substantial differences in the scenario setup and the small subset of CMIP6 models analyzed here. However, comparing the underlying RCP (Taylor et al. 2012; cf. section 2a), Figs. 7b and 7d suggest that the multimodel mean STJ MAX trends from the CCMI-1 REF-C2 runs (RCP6.0) indeed range between the two CMIP6 SSP2-4.5 and SSP5-8.5 projections, which assumed a slightly lower (RCP4.5) and larger (RCP8.5) future increase in global radiative forcing, respectively. Both CMIP6 scenarios project a robust strengthening of the STJ in both hemispheres, with at least doubled trend magnitudes for the extreme SSP5-8.5 setup compared to SSP2-4.5.

Figure 7c shows that, for the multimodel average, the simulations project a robust poleward movement of the subtropical ozone gradient maxima along with the STJ in the SH, again in agreement with our understanding of the underlying ozone transport mechanisms discussed in section 4. The CMIP6 SSP5-8.5 runs show that this shifting becomes stronger upon increased release of greenhouse gases into the atmosphere. In contrast, for the NH, the trends in STJ LAT are less clear among CCMI-1 and CMIP6 (Fig. 7a), and neither are the projected changes in O3GRAD_LMS LAT and TCO LAT, which suggest a robust strengthening and no significant changes in the subtropical ozone gradients, respectively. The latter may be consistent with the significant anticorrelation of TCO LAT with STJ MAX on interannual time scales in ERA5 (cf. Fig. 2), which is indeed reproduced by most of the CCMI-1 models (cf. Fig. 6 and supplemental material), such that TCO LAT would track the counteracting effects of both STJ strengthening and latitudinal jet shifting in the NH.

From the trend analysis of the O3ISO_TTP–3KM metric in Fig. 7, we obtain more divergent results, with some CCMI-1 models showing extreme, rather unrealistic changes in the subtropical ozone gradient magnitudes compared to others and CMIP6. In contrast, trends in O3ISO_TTP–3KM LAT

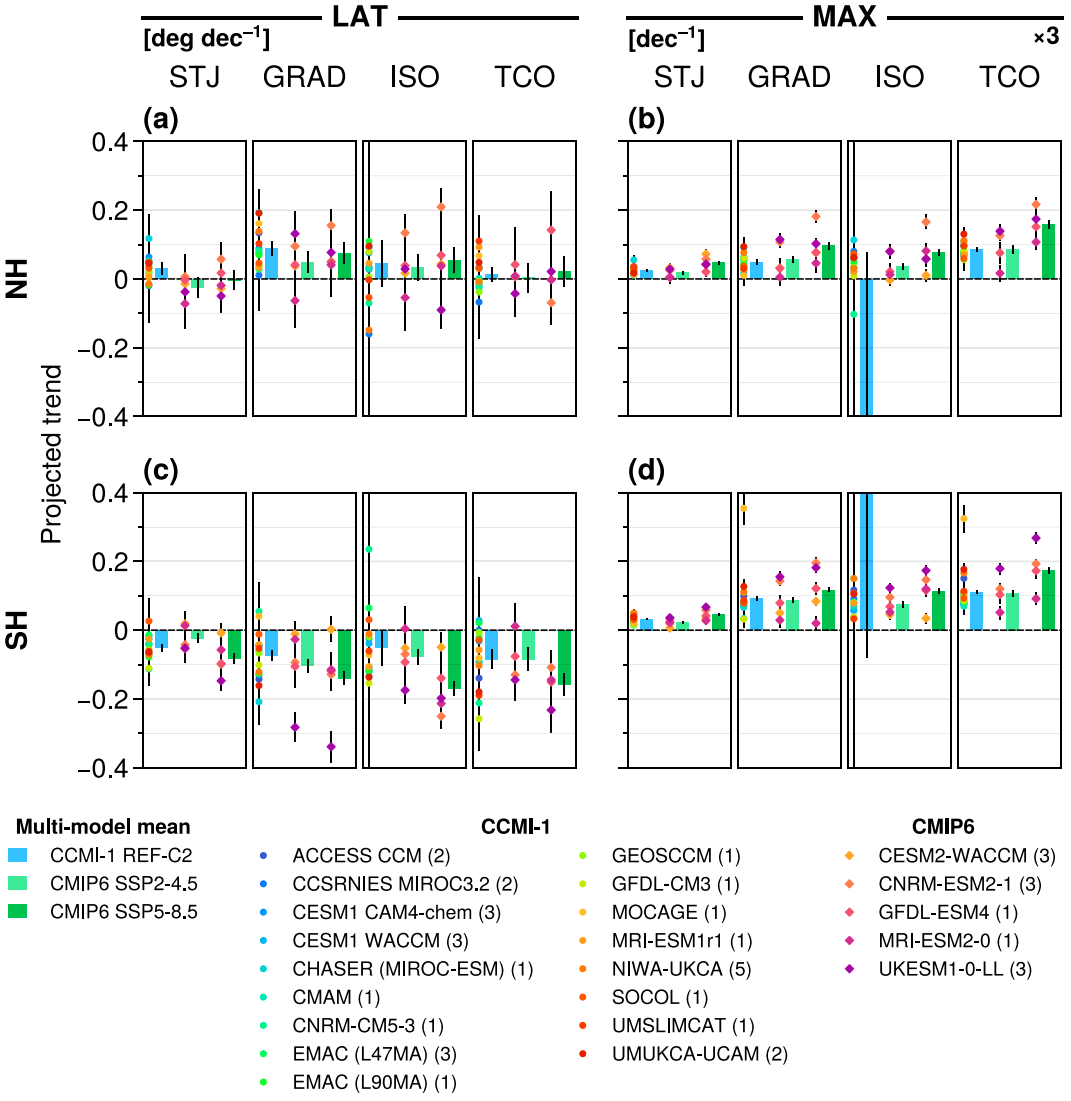

FIG. 7. Projected STJ and ozone gradient trends based on winter-mean data from CCMI-1 (REF-C2) and CMIP6 (SSP2-4.5 and SSP5-8.5) simulations for 2015–98 (NH DJF and SH JJA). Here, the O3GRAD_LMS metric from Table 3 is denoted as "GRAD" and O3ISO_TTP–3KM is abbreviated as "ISO." The models are listed in the legend together with the number of model runs used for computing ensemble-mean linear trends (shown in parentheses each). MMM trends are provided by the vertical bars right next to the individual model markers. Note that the large CCMI-1 MMM trends for ISO MAX are due to outliers that are not fully displayed within (b) and (d). Error bars show 95% confidence intervals for the linear trend regressions. All LAT trends are given in units of °N decade^{-1}, and MAX trends were normalized relative to climatology (1 decade^{-1}, scaled by a factor of 3 for plotting).

turn out to agree better with those derived for O3GRAD_LMS LAT (Figs. 7a,c) and are mostly consistent with the projected changes in the STJ. We assume that the poor performance of the isoline-based metric may sometimes be caused by the limited vertical resolution of the model output (cf. similar issues in analysis with SWOOSH observational data reported in section 5a), indicating potential practical limitations when applying this vertically resolved ozone gradient diagnostic.

Overall, we conclude that CCMI-1 and CMIP6 projections mostly provide evidence for robust coupling of the subtropical jet stream and meridional ozone gradient mean states in extended climate simulations under different external forcing scenarios. While this analysis was based on a multimodel mean framework, Fig. 8 provides an example on STJ–ozone covariability across the individual models considered in this section. In particular, we find robust correlations between the relative strengthening of the STJ and the relative increase in ozone gradient magnitudes in the STJ region in both hemispheres (based on the O3GRAD_LMS ozone gradient metric) across CCMI-1 REF-C2 and the two CMIP6 scenarios. This relationship seems to be slightly weaker in the NH

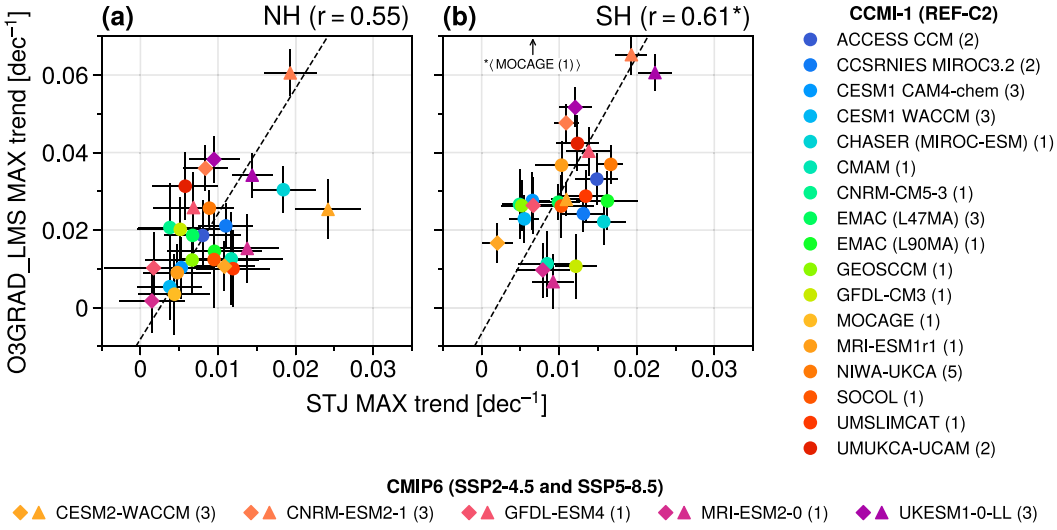

FIG. 8. O3GRAD_LMS MAX ozone gradient trends from CCMI-1 and CMIP6 simulations (NH DJF and SH JJA, 2015–98) plotted against the projected STJ strengthening (STJ MAX), each shown relative to climatology (1 decade^{-1}). Diamond (triangle) markers show the results for the CMIP6 SSP2-4.5 (SSP5-8.5) runs. Note that for the SH, trends obtained from the MOCAGE model projecting an ozone gradient strengthening of approximately 0.12 decade^{-1} (cf. Fig. 7d) are located outside of the figure's panel and therefore are not shown. Cross-model correlation coefficients with p values $p < 0.01$ are provided at the upper-right corner of each panel, where MOCAGE has not been used for the calculation in the SH (correlation coefficient drops to $r = 0.24$ with $p = 0.22$ if this outlier is included). The black dashed lines illustrate orthogonal distance regressions [ODRs; implementation based on `scipy.odr` by Virtanen et al. (2020)] that account for the trend uncertainties in both the predictand and the predictor. Error bars at each model marker show 95% confidence intervals for the trend regressions.

compared to the SH, but overall scales reasonably well with the degree of correlation found for interannual covariability from ERA5 reanalysis data in both hemispheres (cf. Fig. 2). The correlations mainly stem from the correlation across scenarios (i.e., different forcing strength), while the correlation between STJ MAX and O3GRAD_LMS MAX trends across the subset of 17 CCMI-1 models is not statistically significant (not shown). This suggests that the cross-model spread in the CCMI-1 trend projections may be associated with differences in model representations of the STJ–ozone covariability, likely linked to differences in the representation of transport processes.

In general, it is not a priori clear whether a linear relation between the response of the jet stream and meridional ozone gradients in the STJ region holds in a changing climate, in particular for strong climate forcing scenarios where large deviations from the historical mean state of the system are expected. Specifically, in addition to the contribution of horizontal mixing to subtropical ozone variability, indirect effects from other transport processes might amplify or dampen the ozone gradient response to STJ changes. For example, the STJ strength is closely linked to changes in wave driving, which influences both horizontal mixing and the advective transport circulation.

7. Summary and conclusions

In this paper, we investigated whether the distribution of monthly mean zonal-mean ozone in the upper troposphere and lower stratosphere (UTLS) can be used as an indicator of the dynamical variability of large-scale general circulation features. We presented different options for defining ozone-based diagnostics, which each measure the magnitude and meridional position of the maximum zonal-mean ozone gradients located near the subtropical tropopause of both hemispheres.

Using winter-mean ERA5 reanalysis data, we show that this approach yields a robust ozone gradient index, based on either the vertically resolved ozone structure or total-column ozone (TCO) profiles, and is fairly independent of the exact configuration setup. For both hemispheres, we find a close correspondence in interannual variability between the meridional location of the subtropical jet stream (STJ) and the latitude of the maximum ozone gradient in the UTLS region and similar for the jet's zonal wind speed and the sharpness of these gradients. This is consistent with the jet core acting as a barrier for ozone transport governed primarily by wave-induced, quasi-isentropic mixing. Consistently, our results confirm that anomalies in STJ strength and position are coupled with modulations in the meridional gradients of both ozone and potential vorticity. However, advective ozone transport by the mean residual circulation may also indirectly change the magnitude of the ozone gradients as a response to anomalous wave driving (e.g., Abalos et al. 2017, 2020).

Our comparison with vertically resolved ozone observations from the SWOOSH dataset shows good agreement of the results derived from ozone measurements and ERA5 especially in more recent years, when densely sampled satellite

observations allow accurate characterization of the global structure of vertically resolved ozone. Using 40 years of TCO records and the corresponding column ozone metrics, we demonstrate that historical STJ trends may indeed be constrained by observational tracer data and that this indirect approach may allow for further reduction in uncertainties arising from a multireanalysis assessment, provided that long-term and high-quality, global tracer measurements are available. For example, evidence is provided that nonsignificant or diverging results from reanalyses on the historical changes of the NH STJ can be narrowed down by robust trends in the observation-based TCO gradients; i.e., from TCO variations, we infer an annual-mean poleward jet shift of about 0.2° per decade and robust STJ weakening around -0.2 m s^{-1} decade^{-1}.

Finally, from our evaluation of CCMI-1 and selected CMIP6 climate models, we find that recent climate simulations properly reproduce the mode-like correlation signature found in ERA5, i.e., significant covariability within the two groups of diagnostics measuring either the magnitude or latitudinal movement of the STJ core, respectively, and the peak ozone gradients. This is also reflected by mostly consistent STJ and ozone gradient trend signatures obtained from CCMI-1 and CMIP6 climate projections based on different external forcing scenarios.

In conclusion, we showed that changes in zonal-mean ozone in the UTLS can be used to track interannual STJ variability from an atmospheric trace gas distribution in both hemispheres during winter and in the annual mean. Covariability between the STJ and the strong meridional ozone gradients in the STJ region is overall well captured by the two vertically resolved ozone gradient fields analyzed in this work, albeit this approach still suffers from the limited availability of observational ozone data. Additionally, some diverging results from observational records and recent climate simulations, potentially due to the limited vertical resolution of the data used, need to be treated with caution. The underlying metrics, however, are rather intuitive and can be easily brought together with our current understanding of STJ–ozone covariability. In contrast, the usage of TCO-based diagnostics a priori is less clear but indeed allows to constrain historical STJ trends from a much broader range of (observational) datasets. In this sense, potential users of the ozone gradient metrics may apply a combined approach whenever possible and carefully evaluate the underlying STJ–ozone correlations for each individual case.

Since the midlatitude eddy-driven jet (EDJ) is known to be coupled to the STJ through wave-driven dynamics, especially in the NH, this may allow to indirectly estimate EDJ variability from subtropical UTLS ozone. Figure 9 shows the anticorrelation between the STJ magnitude (STJ MAX) and the EDJ's latitudinal position (EDJ LAT) for 1980–2019, which is strong especially during NH winter (DJF) across four different reanalyses (cf. Fig. 2 for ERA5). Likewise, the covariability of EDJ LAT and the ozone gradient strength in the STJ region, as indicated by O3GRAD_LMS, O3ISO_TTP–3KM, and TCO (cf. Table 3), is significant during that time (based on ERA5 data). This could help to constrain interannual EDJ variability from ozone observations and may be compared,

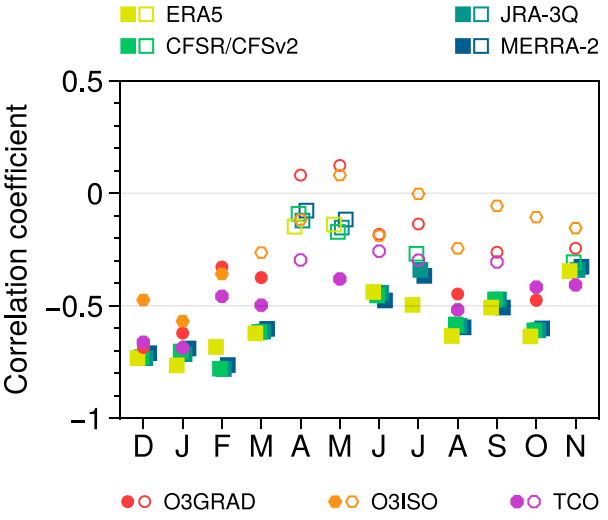

FIG. 9. Seasonal variability of NH correlation between STJ strength (STJ MAX) and EDJ position (EDJ LAT), derived from reanalysis data [1980–2019; S-RIP RID data by Martineau et al. (2018)] and shown by square markers, and ERA5 correlation between EDJ LAT and subtropical ozone gradient magnitudes, as measured by O3GRAD_LMS MAX (round markers), O3ISO_TTP–3KM (hexagons), and TCO MAX (octagons). The filled (open) markers indicate (non)significant correlation values at the 95% level.

e.g., to near-surface zonal wind measurements. We expect the weaker correlations during the summer months in Fig. 9 to arise from both the reduced coupling between the STJ and EDJ as well as from less unique, rather poorly pronounced meridional gradients in the STJ region (cf. appendix). In addition, the EDJ was found to feature a substantial correlation with the meridional mass streamfunction in the troposphere as a relevant metric of tropical width, which was not the case for the STJ (e.g., Davis and Birner 2017; Waugh et al. 2018). This correspondence with the EDJ may be used to further constrain historical tropical expansion trends from observational, ozone-based diagnostics.

We presented a new proxy diagnostic for STJ variability that can be constrained by ozone observations and that serves as a complementary metric of zonal-wind-based metrics from reanalyses, providing support to improve the quantification of essential climate trend signals. Our analysis requires sufficiently strong meridional ozone gradients, which currently limits the application of the ozone gradient metrics to winter-mean and annual-mean data. Climate models show, however, that the underlying subtropical ozone gradients become more pronounced in a future climate, since changes in the STJ wind speeds and midlatitude wave activity can substantially influence UTLS ozone. Future work may also assess other atmospheric trace gases for constructing observation-based metrics of dynamical variability. In particular, long-lived trace species without considerable chemical sources or sinks in the UTLS may be suitable if a sufficient amount of observational data is available and the tracer's distribution features some characteristic

structure that can be continuously linked to the relevant mechanisms of the large-scale general circulation.

Acknowledgments. We thank Molly Menzel and one anonymous reviewer for their comments which significantly helped to improve this paper. We further thank P. Martineau for his support with the S-RIP RID data archive. FH acknowledges helpful discussions with J. Kim (Kongju National University) and P. Rupp (LMU Munich). This research has been supported by the Deutsche Forschungsgemeinschaft (DFG, German Research Foundation)—TRR 301—Project ID 428312742 ("The tropopause region in a changing atmosphere") and by the International Space Science Institute (ISSI) in Bern, Switzerland, through ISSI International Team project No. 460 ("Tropical Width Impacts on the Stratosphere"). We acknowledge the Chemistry–Climate Model Initiative (CCMI) modeling groups for making their simulations available for this analysis, the joint WCRP SPARC/IGAC CCMI for organizing and coordinating the model data analysis activity, and the British Atmospheric Data Centre (BADC) for collecting and archiving the CCMI model output. We further acknowledge the World Climate Research Programme, which, through its Working Group on Coupled Modelling, coordinated and promoted CMIP6. We thank the climate modeling groups for producing and making available their model output, Earth System Grid Federation (ESGF) for archiving the data and providing access, and the multiple funding agencies who support CMIP6 and ESGF. We acknowledge the Python programming language and several additional software extensions therein that were used for computation. Figures have been created using Matplotlib (Hunter 2007), ProPlot (Davis 2021), and various additional color schemes distributed with these packages. We furthermore acknowledge the work by P. Conrat Fuentes (LMU Munich) on Python code for computing thermal tropopause heights that were partially used within this study.

Data availability statement. Hersbach et al. (2023a,b) were downloaded from the Copernicus Climate Change Service (C3S) Climate Data Store (CDS). Additional reanalysis output was obtained from the S-RIP Reanalysis Intercomparison Dataset (RID) at https://www.jamstec.go.jp/ridinfo/, which is an updated version of the data published by Martineau et al. (2018). SWOOSH ozone data by Davis et al. (2016) can be accessed via https://csl.noaa.gov/groups/csl8/swoosh/. ESA Climate Change Initiative MSR data were downloaded from the C3S CDS. TCO data by Bodeker et al. (2021) are available from Bodeker et al. (2022). CCMI-1 model output was published by Hegglin et al. (2015). CMIP6 data were downloaded from the ESGF data network. This work contains modified Copernicus Climate Change Service information. Neither the European Commission nor ECMWF is responsible for any use that may be made of the Copernicus information or data it contains.

APPENDIX

Notes on the Seasonal Cycle

The ozone metrics discussed in section 2 have been constructed such that the subtropical maxima of the underlying ozone gradient fields are clearly pronounced in the resulting latitudinal profiles. From Fig. 1, we find that this works well for all definitions when evaluating their long-term climatology limited to hemispheric winters. However, analyzing full monthly mean data requires to account for the substantial variability induced by the seasonal cycle. As an example, Fig. A1a shows monthly climatologies for the TCO meridional gradient profiles (ERA5, 1979–2023), illustrating regular fluctuations in the locations and strengths of the subtropical gradient maxima throughout the year. In particular, computing the ozone gradient diagnostics turned out to be challenging where unique maxima are missing.

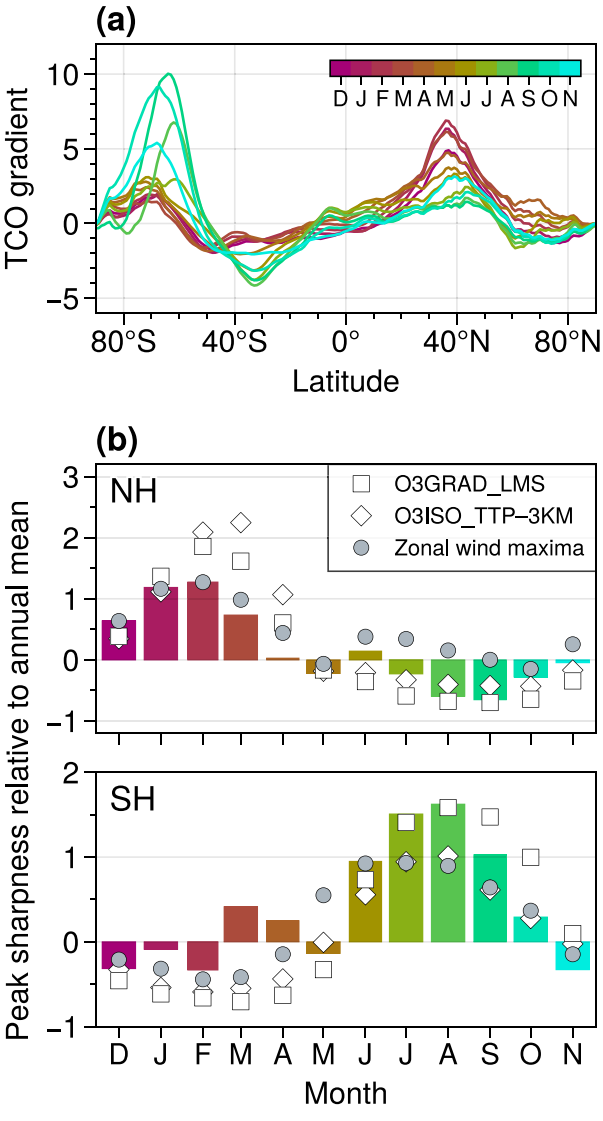

FIG. A1. (a) TCO meridional gradient climatologies (DU deg^{-1}) and as a function of month, based on ERA5 data (1979–2023). (b) Vertical bars illustrate seasonal fluctuations in the subtropical peak shape of the TCO profiles shown in (a) according to the peak sharpness measure defined in Eq. (1), calculated for each hemisphere separately. The white and gray markers show this cycle for the remaining two ozone gradient definitions and for the STJs' zonal-mean zonal wind vertical shear maxima, respectively.

We may quantify this finding by defining a "peak sharpness" $P(m)$ as the ratio between the absolute magnitude of the subtropical gradient maximum and its full width at half maximum for a given monthly climatology $m = 1, 2, \ldots, 12$. Then, the dimensionless measure,

$$\frac{P(m)}{P_{\text{clim}}} - 1, \tag{A1}$$

gives an estimate of the seasonal variation of the peak sharpness relative to the annual-mean climatology P_{clim}. For example, if $P(m) > P_{\text{clim}}$, the subtropical ozone maximum is better pronounced during month m than for the annual mean, and thus, peak-based metrics may be more robust during this month. Figure A1b provides this peak sharpness measure defined in Eq. (A1) for the different ozone gradient profiles as a function of month m. We note a clear seasonal cycle for all ozone-based metrics, suggesting enhanced "performance" during winter and early spring on each hemisphere. Furthermore, it turns out that the zonal-mean zonal wind vertical shear maxima, as constructed for the STJ LAT metric described in Table 2, show a similar, albeit less strongly pronounced, behavior. The peak sharpness may be additionally weakened by local monsoon effects during summer on the NH. This suggests that in general our findings need to be treated with caution if they potentially result from less unique structures of the zonal-mean variable fields.

REFERENCES

Abalos, M., and A. de la Cámara, 2020: Twenty-first century trends in mixing barriers and eddy transport in the lower stratosphere. *Geophys. Res. Lett.*, **47**, e2020GL089548, https://doi.org/10.1029/2020GL089548.

——, W. J. Randel, D. E. Kinnison, and R. R. Garcia, 2017: Using the artificial tracer e90 to examine present and future UTLS tracer transport in WACCM. *J. Atmos. Sci.*, **74**, 3383–3403, https://doi.org/10.1175/JAS-D-17-0135.1.

——, and Coauthors, 2020: Future trends in stratosphere-to-troposphere transport in CCMI models. *Atmos. Chem. Phys.*, **20**, 6883–6901, https://doi.org/10.5194/acp-20-6883-2020.

Adam, O., and Coauthors, 2018a: The TropD software package (v1): Standardized methods for calculating tropical-width diagnostics. *Geosci. Model Dev.*, **11**, 4339–4357, https://doi.org/10.5194/gmd-11-4339-2018.

——, and Coauthors, 2018b: TropD: Tropical width diagnostics software package. Zenodo, https://doi.org/10.5281/zenodo.1157043.

Bodeker, G. E., J. Nitzbon, J. S. Tradowsky, S. Kremser, A. Schwertheim, and J. Lewis, 2021: A global total column ozone climate data record. *Earth Syst. Sci. Data*, **13**, 3885–3906, https://doi.org/10.5194/essd-13-3885-2021.

——, S. Kremser, and J. S. Tradowsky, 2022: BS filled total column ozone database V3.4.1. Zenodo, accessed 10 January 2024, https://doi.org/10.5281/zenodo.7447757.

Cariolle, D., and H. Teyssèdre, 2007: A revised linear ozone photochemistry parameterization for use in transport and general circulation models: Multi-annual simulations. *Atmos. Chem. Phys.*, **7**, 2183–2196, https://doi.org/10.5194/acp-7-2183-2007.

Chemke, R., and J. Yuval, 2023: Human-induced weakening of the Northern Hemisphere tropical circulation. *Nature*, **617**, 529–532, https://doi.org/10.1038/s41586-023-05903-1.

Copernicus Climate Change Service, 2020: Ozone monthly gridded data from 1970 to present derived from satellite observations. Copernicus Climate Change Service (C3S) Climate Data Store (CDS), accessed 8 January 2024, https://doi.org/10.24381/cds.4ebfe4eb.

Davis, L. L. B., 2021: ProPlot Version v0.9.5. Zenodo, https://doi.org/10.5281/zenodo.3873878.

Davis, N., and T. Birner, 2017: On the discrepancies in tropical belt expansion between reanalyses and climate models and among tropical belt width metrics. *J. Climate*, **30**, 1211–1231, https://doi.org/10.1175/JCLI-D-16-0371.1.

Davis, N. A., and T. Birner, 2013: Seasonal to multidecadal variability of the width of the tropical belt. *J. Geophys. Res. Atmos.*, **118**, 7773–7787, https://doi.org/10.1002/jgrd.50610.

Davis, S. M., and Coauthors, 2016: The Stratospheric Water and Ozone Satellite Homogenized (SWOOSH) database: A long-term database for climate studies. *Earth Syst. Sci. Data*, **8**, 461–490, https://doi.org/10.5194/essd-8-461-2016.

——, B. Hassler, and K. H. Rosenlof, 2018: Revisiting ozone measurements as an indicator of tropical width. *Prog. Earth Planet. Sci.*, **5**, 56, https://doi.org/10.1186/s40645-018-0214-5.

——, and Coauthors, 2022: Overview of ozone and water vapour. SPARC Reanalysis Intercomparison Project (S-RIP) Final Rep. SPARC Rep. 10, WCRP-17/2020, 123–164, https://doi.org/10.17874/800dee57d13.

ECMWF, 2016: Part IV: Physical processes. IFS Documentation CY41R2, ECMWF, 213 pp., https://doi.org/10.21957/tr5rv27xu.

Eyring, V., and Coauthors, 2013: Overview of IGAC/SPARC Chemistry-Climate Model Initiative (CCMI) community simulations in support of upcoming ozone and climate assessments. *SPARC Newsletter*, No. 40, SPARC Office, Toronto, Ontario, Canada, 48–66, https://www.aparc-climate.org/publications/newsletter/.

——, S. Bony, G. A. Meehl, C. A. Senior, B. Stevens, R. J. Stouffer, and K. E. Taylor, 2016: Overview of the Coupled Model Intercomparison Project Phase 6 (CMIP6) experimental design and organization. *Geosci. Model Dev.*, **9**, 1937–1958, https://doi.org/10.5194/gmd-9-1937-2016.

Grise, K. M., and Coauthors, 2019: Recent tropical expansion: Natural variability or forced response? *J. Climate*, **32**, 1551–1571, https://doi.org/10.1175/JCLI-D-18-0444.1.

Hegglin, M. I., J. F. Lamarque, and V. Eyring, 2015: The IGAC/SPARC Chemistry-Climate Model Initiative Phase-1 (CCMI-1) model data output. NCAS British Atmospheric Data Centre, accessed 30 January 2025, https://catalogue.ceda.ac.uk/uuid/9cc6b94df0f4469d8066d69b5df879d5.

Hersbach, H., and Coauthors, 2020: The ERA5 global reanalysis. *Quart. J. Roy. Meteor. Soc.*, **146**, 1999–2049, https://doi.org/10.1002/qj.3803.

——, and Coauthors, 2023a: ERA5 monthly averaged data on pressure levels from 1940 to present. Copernicus Climate Change Service (C3S) Climate Data Store (CDS), accessed 24 April 2024, https://doi.org/10.24381/cds.6860a573.

——, and Coauthors, 2023b: ERA5 monthly averaged data on single levels from 1940 to present. Copernicus Climate Change Service (C3S) Climate Data Store (CDS), accessed 25 April 2024, https://doi.org/10.24381/cds.f17050d7.

Hudson, R. D., 2012: Measurements of the movement of the jet streams at mid-latitudes, in the Northern and Southern

Hemispheres, 1979 to 2010. *Atmos. Chem. Phys.*, **12**, 7797–7808, https://doi.org/10.5194/acp-12-7797-2012.

——, A. D. Frolov, M. F. Andrade, and M. B. Follette, 2003: The total ozone field separated into meteorological regimes. Part I: Defining the regimes. *J. Atmos. Sci.*, **60**, 1669–1677, https://doi.org/10.1175/1520-0469(2003)060<1669:TTOFSI>2.0.CO;2.

——, M. F. Andrade, M. B. Follette, and A. D. Frolov, 2006: The total ozone field separated into meteorological regimes—Part II: Northern Hemisphere mid-latitude total ozone trends. *Atmos. Chem. Phys.*, **6**, 5183–5191, https://doi.org/10.5194/acp-6-5183-2006.

Hunter, J. D., 2007: Matplotlib: A 2D graphics environment. *Comput. Sci. Eng.*, **9**, 90–95, https://doi.org/10.1109/MCSE.2007.55.

Keeble, J., and Coauthors, 2021: Evaluating stratospheric ozone and water vapour changes in CMIP6 models from 1850 to 2100. *Atmos. Chem. Phys.*, **21**, 5015–5061, https://doi.org/10.5194/acp-21-5015-2021.

Lait, L. R., 1994: An alternative form for potential vorticity. *J. Atmos. Sci.*, **51**, 1754–1759, https://doi.org/10.1175/1520-0469(1994)051<1754:AAFFPV>2.0.CO;2.

Lee, J.-Y., and Coauthors, 2021: Future global climate: Scenario-based projections and near-term information. *Climate Change 2021: The Physical Science Basis*, V. Masson-Delmotte et al., Eds., Cambridge University Press, 553–672, https://doi.org/10.1017/9781009157896.006.

Lee, S., and H.-K. Kim, 2003: The dynamical relationship between subtropical and eddy-driven jets. *J. Atmos. Sci.*, **60**, 1490–1503, https://doi.org/10.1175/1520-0469(2003)060<1490:TDRBSA>2.0.CO;2.

Leith, C. E., 1975: Climate response and fluctuation dissipation. *J. Atmos. Sci.*, **32**, 2022–2026, https://doi.org/10.1175/1520-0469(1975)032<2022:CRAFD>2.0.CO;2.

Limpasuvan, V., and D. L. Hartmann, 1999: Eddies and the annular modes of climate variability. *Geophys. Res. Lett.*, **26**, 3133–3136, https://doi.org/10.1029/1999GL010478.

Long, C., M. Fujiwara, S. Davis, D. Mitchell, and C. Wright, 2022: Overview of temperature and winds. SPARC Reanalysis Intercomparison Project (S-RIP) Final Rep. SPARC Rep. 10, WCRP-17/2020, 81–122, https://doi.org/10.17874/800dee57d13.

Long, C. S., M. Fujiwara, S. Davis, D. M. Mitchell, and C. J. Wright, 2017: Climatology and interannual variability of dynamic variables in multiple reanalyses evaluated by the SPARC Reanalysis Intercomparison Project (S-RIP). *Atmos. Chem. Phys.*, **17**, 14593–14629, https://doi.org/10.5194/acp-17-14593-2017.

Lorenz, D. J., and D. L. Hartmann, 2001: Eddy–zonal flow feedback in the Southern Hemisphere. *J. Atmos. Sci.*, **58**, 3312–3327, https://doi.org/10.1175/1520-0469(2001)058<3312:EZFFIT>2.0.CO;2.

——, and ——, 2003: Eddy–zonal flow feedback in the Northern Hemisphere winter. *J. Climate*, **16**, 1212–1227, https://doi.org/10.1175/1520-0442(2003)16<1212:EFFITN>2.0.CO;2.

Martineau, P., J. S. Wright, N. Zhu, and M. Fujiwara, 2018: Zonal-mean data set of global atmospheric reanalyses on pressure levels. *Earth Syst. Sci. Data*, **10**, 1925–1941, https://doi.org/10.5194/essd-10-1925-2018.

Meinshausen, M., and Coauthors, 2020: The shared socioeconomic pathway (SSP) greenhouse gas concentrations and their extensions to 2500. *Geosci. Model Dev.*, **13**, 3571–3605, https://doi.org/10.5194/gmd-13-3571-2020.

Menzel, M. E., D. Waugh, and K. Grise, 2019: Disconnect between Hadley cell and subtropical jet variability and response to increased CO_2. *Geophys. Res. Lett.*, **46**, 7045–7053, https://doi.org/10.1029/2019GL083345.

——, D. W. Waugh, Z. Wu, and T. Reichler, 2024: Replicating the Hadley cell edge and subtropical jet latitude disconnect in idealized atmospheric models. *Wea. Climate Dyn.*, **5**, 251–261, https://doi.org/10.5194/wcd-5-251-2024.

Ming, A., 2022: PyTropD version 2.12. GitHub, accessed 6 February 2024, https://github.com/TropD/pytropd.

Morgenstern, O., and Coauthors, 2017: Review of the global models used within phase 1 of the Chemistry–Climate Model Initiative (CCMI). *Geosci. Model Dev.*, **10**, 639–671, https://doi.org/10.5194/gmd-10-639-2017.

O'Neill, B. C., and Coauthors, 2016: The Scenario Model Intercomparison Project (ScenarioMIP) for CMIP6. *Geosci. Model Dev.*, **9**, 3461–3482, https://doi.org/10.5194/gmd-9-3461-2016.

Riahi, K., and Coauthors, 2017: The Shared Socioeconomic Pathways and their energy, land use, and greenhouse gas emissions implications: An overview. *Global Environ. Change*, **42**, 153–168, https://doi.org/10.1016/j.gloenvcha.2016.05.009.

Schneider, T., 2006: The general circulation of the atmosphere. *Annu. Rev. Earth Planet. Sci.*, **34**, 655–688, https://doi.org/10.1146/annurev.earth.34.031405.125144.

Shaw, T. A., 2019: Mechanisms of future predicted changes in the zonal mean mid-latitude circulation. *Curr. Climate Change Rep.*, **5**, 345–357, https://doi.org/10.1007/s40641-019-00145-8.

——, and O. Miyawaki, 2024: Fast upper-level jet stream winds get faster under climate change. *Nat. Climate Change*, **14**, 61–67, https://doi.org/10.1038/s41558-023-01884-1.

——, and Coauthors, 2024: Emerging climate change signals in atmospheric circulation. *AGU Adv.*, **5**, e2024AV001297, https://doi.org/10.1029/2024AV001297.

Shepherd, T. G., and C. McLandress, 2011: A robust mechanism for strengthening of the Brewer–Dobson circulation in response to climate change: Critical-layer control of subtropical wave breaking. *J. Atmos. Sci.*, **68**, 784–797, https://doi.org/10.1175/2010JAS3608.1.

Staten, P. W., J. Lu, K. M. Grise, S. M. Davis, and T. Birner, 2018: Re-examining tropical expansion. *Nat. Climate Change*, **8**, 768–775, https://doi.org/10.1038/s41558-018-0246-2.

Taylor, K. E., R. J. Stouffer, and G. A. Meehl, 2012: An overview of CMIP5 and the experiment design. *Bull. Amer. Meteor. Soc.*, **93**, 485–498, https://doi.org/10.1175/BAMS-D-11-00094.1.

Thompson, D. W. J., and J. M. Wallace, 1998: The Arctic Oscillation signature in the wintertime geopotential height and temperature fields. *Geophys. Res. Lett.*, **25**, 1297–1300, https://doi.org/10.1029/98GL00950.

——, and ——, 2000: Annular modes in the extratropical circulation. Part I: Month-to-month variability. *J. Climate*, **13**, 1000–1016, https://doi.org/10.1175/1520-0442(2000)013<1000:AMITEC>2.0.CO;2.

Totz, S., S. Petri, J. Lehmann, and D. Coumou, 2018: Regional changes in the mean position and variability of the tropical edge. *Geophys. Res. Lett.*, **45**, 12 076–12 084, https://doi.org/10.1029/2018GL079911.

Vallis, G. K., P. Zurita-Gotor, C. Cairns, and J. Kidston, 2015: Response of the large-scale structure of the atmosphere to global warming. *Quart. J. Roy. Meteor. Soc.*, **141**, 1479–1501, https://doi.org/10.1002/qj.2456.

Van Roozendael, M., and Coauthors, 2021a: Ozone Algorithm Theoretical Basis Document (ATBD), version 2.1. Copernicus Climate Change Service, accessed 2 May 2025, https://dast.copernicus-climate.eu/documents/satellite-ozone/C3S2_312b_

Lot2_2024/C3S2_312a_Lot2_D-WP2_FDDP-PQAR_202311_O3_v3.3_final.pdf.

——, and Coauthors, 2021b: Ozone Product User Guide and Specification (PUGS), version 2.1. Copernicus Climate Change Service, accessed 2 May 2025, https://dast.copernicus-climate.eu/documents/satellite-ozone/C3S2_312b_Lot2_2024/C3S2_312a_Lot2_D-WP2-FDDP-PUGS_202311_O3_v3.5_final.pdf.

Virtanen, P., and Coauthors, 2020: Scipy 1.0: Fundamental algorithms for scientific computing in Python. *Nat. Methods*, **17**, 261–272, https://doi.org/10.1038/s41592-019-0686-2.

Waters, J. W., and Coauthors, 2006: The Earth observing system microwave limb sounder (EOS MLS) on the aura satellite. *IEEE Trans. Geosci. Remote Sens.*, **44**, 1075–1092, https://doi.org/10.1109/TGRS.2006.873771.

Waugh, D. W., and Coauthors, 2018: Revisiting the relationship among metrics of tropical expansion. *J. Climate*, **31**, 7565–7581, https://doi.org/10.1175/JCLI-D-18-0108.1.

WMO, 1957: Meteorology—A three-dimensional science. Second session of the Commission for Aerology. *WMO Bull.*, **6**, 134–138.

——, 2011: Scientific assessment of ozone depletion: 2010. Global Ozone Research and Monitoring Project Rep. 52, WMO, 442 pp.

Woollings, T., 2016: Storm tracks, blocking, and climate change: A review. *Dynamics and Predictability of Large-Scale, High-Impact Weather and Climate Events*, J. Li et al., Eds., Cambridge University Press, 113–121, https://doi.org/10.1017/CBO9781107775541.009.

——, M. Drouard, C. H. O'Reilly, D. M. H. Sexton, and C. McSweeney, 2023: Trends in the atmospheric jet streams are emerging in observations and could be linked to tropical warming. *Commun. Earth Environ*, **4**, 125, https://doi.org/10.1038/s43247-023-00792-8.

Zappa, G., 2019: Regional climate impacts of future changes in the mid-latitude atmospheric circulation: A storyline view. *Curr. Climate Change Rep.*, **5**, 358–371, https://doi.org/10.1007/s40641-019-00146-7.